Title

A statistical analysis of avalanching heat transport in stationary enhanced core confinement regimes

Authors

Tokunaga, S
Jhang, Hogun
Kim, SS
et al.

Peer reviewed

A statistical analysis of avalanching heat transport in stationary enhanced core confinement regimes

S. Tokunaga,[1,a)] Hogun Jhang,[1,b)] S. S. Kim,[1] and P. H. Diamond[1,2]

[1]*WCI Center for Fusion Theory, National Fusion Research Institute, 52, Yeoeun-dong, Yusung-Gu, Daejon, South Korea*
[2]*Center for Astrophysics and Space Sciences and Department of Physics, University of California San Diego, La Jolla, California 92093-0429, USA*

We present a statistical analysis of heat transport in stationary enhanced confinement regimes obtained from flux-driven gyrofluid simulations. The probability density functions of heat flux in improved confinement regimes, characterized by the Nusselt number, show significant deviation from Gaussian, with a markedly fat tail, implying the existence of heat avalanches. Two types of avalanching transport are found to be relevant to stationary states, depending on the degree of turbulence suppression. In the weakly suppressed regime, heat avalanches occur in the form of quasi-periodic (QP) heat pulses. Collisional relaxation of zonal flow is likely to be the origin of these QP heat pulses. This phenomenon is similar to transient limit cycle oscillations observed prior to edge pedestal formation in recent experiments. On the other hand, a spectral analysis of heat flux in the strongly suppressed regime shows the emergence of a $1/f$ (f is the frequency) band, suggesting the presence of self-organized criticality (SOC)-like episodic heat avalanches. This episodic $1/f$ heat avalanches have a long temporal correlation and constitute the dominant transport process in this regime. © 2012 American Institute of Physics. [http://dx.doi.org/10.1063/1.4752218]

I. INTRODUCTION

Realization of advanced tokamak operation in ITER and future reactors requires operating a plasma in stationary enhanced confinement regime, likely characterized by the existence of core transport barriers. The present paradigm is that the formation of transport barriers either internal (internal transport barrier, ITB[1,2]) or edge (edge transport barrier, ETB[3,4]) is a consequence of the development of the strong $E \times B$ shear, giving rise to the reduction or even quench of *local* turbulent transport via eddy decorrelation of turbulence.[5,6] Then, the anomalous transport due to plasma turbulence is reduced, and the role of irreducible neoclassical transport becomes more important in an improved confinement regime.

Experiments[7–12] and numerical simulations[13–17] have often shown the existence of *non-local* heat avalanches in magnetically confined plasmas, in addition to local diffusive transport. In particular, a recent gyrokinetic simulation study highlights one self-organization process, which can determine transport: the prevalence of self-organized, avalanche-dominated transport on mesoscales (with a Lorentzian kernel), and the persistence of static $E \times B$ staircases, the spacing of which defines the outer scale of the avalanche distribution.[18] Here, "mesoscale" is defined as the range of scales (ΔL) between the turbulent eddy size (L_{corr}) and the macroscopic system size (L), i.e., $L_{corr} < \Delta L < L$. These heat avalanches usually have long spatio-temporal correlations, far beyond the turbulence eddy decorrelation length and time. A natural conse-

quence of the existence of avalanching heat transport would be the breaking of the local mixing length-type gyroBohm transport scaling,[19] in particular when turbulence spreading or avalanches exists (In practice, avalanches and turbulence spreading are coupled each other and hardly discernible, as pointed out in a recent paper[20]). Then, it is likely that the degree of departure from the gyroBohm scaling may depend on the relative impact of non-local transport as compared to diffusive transport.

Heat avalanches in fusion plasmas show similarity to self-organized criticality (SOC)[21] phenomena where avalanches develop and propagate as a consequence of a local temperature gradient, which exceeds the local threshold.[22–24] Typically, the heat avalanches are intermittent bursty transport events with long spatio-temporal correlations, and characterized by the appearance of $1/f$ power spectrum,[7,8,10] where f is the frequency. A running sandpile model[25] has often been invoked to study the essential physics features of SOC-like avalanches in fusion plasmas.[23,26–29]

In numerical simulations, many papers have been devoted to the study of avalanching heat transport in magnetically confined plasmas with varying degrees of numerical sophistication.[13,18,30–32] Many features of heat avalanches were studied, for instance, the scaling of the propagation speed of a heat pulse,[15–17] the long range spatio-temporal correlations,[18] and the appearance of a $1/f$ power spectrum.[31] However, the physics of avalanching heat transport has not been fully explored so far, especially in the context of a self-consistently generated enhanced confinement regime. This is because most of previous numerical studies considered either *conventional* plasmas without confinement improvement, or simulated enhanced confinement regimes generated by externally imposed strong $E \times B$ shear. In fact, few self-consistent

a)Present address: Research Organization for Information Science and Technology (RIST), 2-4, Shirakata, Tokai-mura, Naka-gun, Ibaraki-ken 319-1106, Japan.
b)Electronic mail: hgjhang@nfri.re.kr.

numerical studies are available in the literature, which report the detailed characteristics of avalanching heat transport in plasmas with stationary, flux-driven transport barriers.

The primary objective of this paper is to investigate the characteristics of avalanching heat transport in a stationary tokamak plasma in a self-consistently generated enhanced confinement regime. In particular, we are interested in possible qualitative change in the avalanching heat transport process, as an ITB evolves from a weak to strong one. Beyer *et al.* and Benkadda *et al.* addressed this issue based on fluid resistive ballooning turbulence simulations in slab geometry.[31,32] In these studies, they pointed out some possible characteristics of avalanching, such as the change of heat flux power spectrum due to self-consistent zonal flow,[31] (i.e., the appearance of 1/f frequency band) and the properties of a heat avalanche when strong external shear flow is imposed.[32] Also, possible aspects of avalanching in externally prescribed transport barriers were studied in some sandpile simulations, showing the appearance of long temporal correlations with a power law quiet time distribution (QTD) in a bistable sandpile model,[27] and the appearance of a 1/f frequency regime when diffusive transport is strongly reduced in a diffusive sandpile model.[33] To our knowledge, however, no published result addresses the characteristics of avalanching heat transport in stationary ITB produced by self-consistent flux-driven numerical simulations with ion temperature gradient (ITG) driven turbulence in toroidal geometry. We remark in passing that this study is of interest in ITER steady state operation with core transport barriers because of its potential implications for transport scaling. If the fraction of non-local transport is significant in comparison with diffusive one, it is quite likely that gyroBohm scaling will be broken.

To study avalanching heat transport numerically, it is necessary to exploit global, long-time simulations. The requirement of global simulations is obvious: we study non-local avalanching which can support a long spatial correlation. The long-time (longer than at least 100 energy confinement times) simulation capability is also requested to obtain a stationary state with statistically meaningful data. In this sense, global gyrofluid simulations are useful, due to rapid computational speed while keeping the minimal physics in plasma turbulence. In this work, we use a revised version of the TRB code.[34,35] The main drawback of our numerical model is that it retains only resonant modes, which is problematic near the $dq(r)/dr = 0$ region ($q(r)$: the safety factor profile) where non-resonant modes play an important role.[36,37] The difficulty in generating transport barriers in reversed magnetic shear using self-consistent flux-driven simulations has been attributed to the presence of non-resonant modes, even though the physics of how non-resonant modes prevent barrier formation has not been fully elucidated. In spite of this limitation, however, the present numerical model still has merits for studying aspects of transport barrier physics, given a proper analysis of the simulation data. In particular, the reader should note that this paper deals with the scaling characteristics of the turbulent flux, and not with the quantitative details of internal transport barrier thresholds and formation.

The remainder of this paper is organized as follows: In Sec. II, we present features of our numerical simulations:

global flux-driven simulations using the TRB code. After a brief introduction of a numerical model being used in this paper, we present characteristics of stationary, flux-driven enhanced confinement states. We parametrize the degree of turbulence suppression in the enhanced confinement region in terms of a Nusselt number, Nu, which is averaged over the duration of the steady state. We then introduce two representative enhanced confinement states, each representing a weak and a strong suppression regime. In Sec. III, we perform a statistical analysis of heat transport in the stationary improved confinement regime obtained from gyrofluid simulations. After examining the heat flux probability density functions (PDF) at enhanced confinement layers, we perform a frequency spectrum analysis. The power spectral density (PSD) of the heat flux is shown to undergo a dramatic change as Nusselt number decreases, (i.e., when turbulence is strongly suppressed). Most notable is the appearance of an SOC-like broad 1/f frequency region. We evaluate the amount of heat transport resulting from heat avalanches by calculating the frequency-resolved heat flux, which reveals that a significant fraction of heat flux comes from heat avalanches. Section IV is devoted to the detailed study of the characteristics of heat avalanches in the representative enhanced confinement states using a statistical correlation analysis. We show that heat avalanches in the weakly suppressed regime (i.e., when Nusselt number is high) appear as quasi-periodic (QP) heat pulses, which are associated with relaxation oscillations of zonal flows at the shoulder location of the enhanced confinement layer. We present a physics picture of how quasi-periodic heat pulses discharge excess heat out of the enhanced confinement region. Evaluation of both a quiet time distribution and Hurst exponents shows that episodic heat avalanches, which are responsible for the appearance of the 1/f frequency region of PSD in the strongly suppressed regime, have a long temporal correlation. We conclude this paper in Sec. V with a brief summary of main results and some discussions.

II. GLOBAL GYROFLUID SIMULATIONS OF FLUX-DRIVEN PLASMAS WITH ENHANCED CONFINEMENT

In this section, we perform a set of long time global gyrofluid simulations to obtain fully flux-driven steady states with improved confinement regions. A gyrofluid model based on the TRB code[34] is used for this study. For completeness, we first briefly mention features of the simulation model of the revised TRB code.[35] Then, we describe characteristics of stationary states with improved confinement regions obtained from the simulations.

A. Simulation model

We study electrostatic ITG turbulence using a three-field gyrofluid model consisting of vorticity, parallel flow, and pressure balance equations,

$$(d_t - D_{\text{vis}} - D_{\text{neo}})\Omega = -n_i \nabla_\| V_\| + 2n_i(\mathbf{V}_E + \mathbf{V}_{p_i}) \cdot \nabla \ln B$$
$$+ n_i \mathbf{V}_{p_i} \cdot \nabla\left(\frac{\tilde{n}_i - \Omega}{n_i}\right) - d_t \hat{n}_i, \quad (1)$$

$$(d_t - D_{\text{vis}})V_\| = -\frac{e}{m_i}\nabla_\|\varphi - \frac{1}{m_i n_i}\nabla_\| p_i, \qquad (2)$$

$$(d_t - D_{\text{vis}} - D_{\text{glf}})p_i = \frac{10}{3}p_i\mathbf{V}_{T_i}\cdot\nabla\ln B + \frac{5}{3}T_i d_t n_i + S_p, \qquad (3)$$

where n_i, T_i (p_i), φ, and $V_\|$ are the ion density, temperature (pressure), potential, and parallel flow, respectively, $d_t = \partial/\partial t + \mathbf{V}_E\cdot\nabla$, D_{vis}, D_{neo}, and D_{glf} represent viscous dissipation, neoclassical friction, and Landau damping operator,[34] respectively. Here, $\Omega = \tilde{n}_i - (cn_i/\omega_{ci}B)\nabla_\perp^2\varphi$ is a generalized vorticity, $\mathbf{V}_E$ and $\mathbf{V}_{p_i}$ are $E \times B$ and ion diamagnetic drift velocities, $\mathbf{V}_{T_i} = \frac{\mathbf{B}\times\nabla T_i}{m_i\omega_{ci}B}$. S_p denotes ion heat source. The "hat" notation means a flux surface average, $\hat{F}(r,t) = \int d\theta d\phi F(r,\theta,\phi,t)/4\pi^2$, and $\tilde{F} = F - \hat{F}$ for any quantity F. A circular tokamak equilibrium and adiabatic response of electrons (i.e., $\tilde{n}_i = \tilde{n}_e = en_e\tilde{\varphi}/T_e$) are assumed. We prescribe both the collisional diffusivity in D_{vis} and neoclassical damping coefficient in D_{neo}, which is chosen in accordance with the other plasma parameters being used. In subsequent simulations throughout the paper, we fix the safety factor profile $q(r)$ with off-axis q_{min} (i.e., reversed magnetic shear), as shown in Fig. 1(a) together with the position of resonant surfaces. We retain only resonant modes, which are radially localized around rational surfaces $r = r_{mn}$ defined as $q(r_{mn}) = m/n$. The limitation of the present numerical model caused by taking only resonant modes was already discussed in Sec. I. Figure 1(b) shows the profiles for electron density and temperature being used in simulations in this paper. The density profile is almost flat throughout the plasma. Both profiles are also fixed in time during all the simulations.
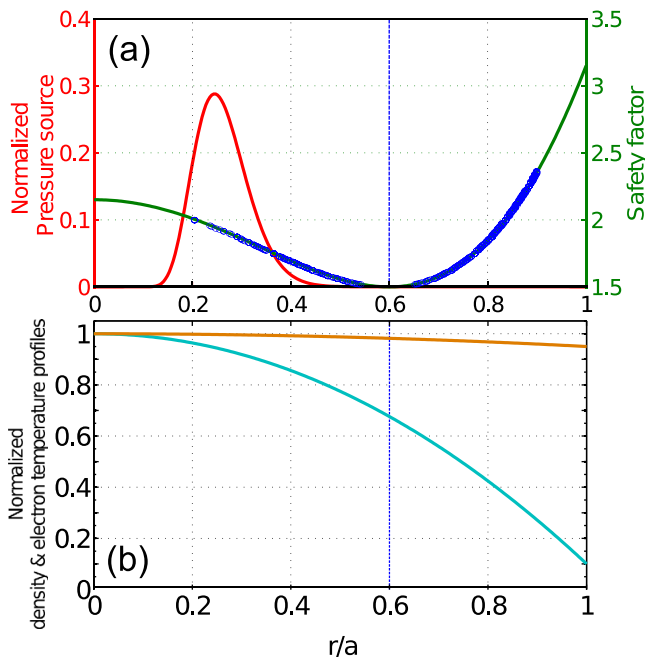

FIG. 1. (a) Radial profiles of safety factor $q(r)$ (green) and normalized pressure (heat) source (red). Blue points in $q(r)$ represent the position of resonant surfaces. (b) Radial profiles of density and electron temperature. They are fixed in time in all the simulations presented in this paper.

The density and temperature are normalized by reference values n_0 and T_0, respectively. These reference values do not evolve in time and are given in terms of simulation parameters, as will be shown shortly. Other quantities related to these are $c_s = T_0/m_i$ and $\rho_{i0} = m_i c_s/eB$. Figure 1(a) also show the radial profile of a heat source (red solid line) being used in our simulations. It has a peak at $r/a = \rho \sim 0.25$. We fix this heat deposition profile in all the subsequent simulations, while varying the amplitude of the heat source. The total power absorbed by ions, P_{tot}, is related to the amplitude of the heat source and given by $P_{tot} = 6\pi^2 Ra^2\langle S_p\rangle$, where R (a) is the major (minor) radius, and $\langle S_p\rangle = \int_0^1 S_p(r)dr$. We use the normalized value of $\langle S_p\rangle$ given by $\langle S_p\rangle = S_0\rho_* n_0 T_0/t_0$, where ρ_* is the normalized gyroradius. Hereafter, we use S_0 to represent the strength of the heat source. The total input power P_{tot} is determined by choosing S_0 for fixed values of ρ_*, R, n_0, and T_0. For example, choosing $\rho_* = 0.006$, $n_0 = 1.0 \times 10^{20}$ m^{-3}, $T_0 = 3$ keV, $R = 1\,m$, and $S_0 = 0.004$ gives $P_{tot} \approx 9.8$ MW. From now on, we take these numbers as reference values, if not specified explicitly.

B. Flux-driven plasmas with enhanced confinement

We perform a set of long time TRB simulations to identify basic characteristics of flux-driven steady state plasmas with reversed magnetic shear. A heat source (S_p in Eq. (3)) is used to sustain and vary the heat flux while the ion temperature and parallel flow profiles evolve self-consistently. The heat source deposits a constant power input distribution centred at $r/a = \rho \sim 0.25$, as shown in Fig. 1(a). All the simulations start with a plasma with a flat ion temperature profile.

Figure 2 shows time trajectories for turbulent heat flux (Q_i) vs. ion temperature gradient ($-\nabla T_i$) at improved confinement regions, which are formed self-consistently in vicinity of the q-minimum position. We take a time overage over the period $\Delta t = 2000$ a/c_s to obtain each trajectory in Fig. 2. Ion temperature increases gradually as a result of central heating and undergoes a sudden transition to form an ITB-like profile, due to the reduction of turbulent transport. It remains in a steady state with constant heat flux at the enhanced confinement region, i.e., in a flux-driven state. The variation of ∇T_i at steady states is achieved by changing the power of a central heat source, as shown in Fig. 2. To obtain flux-driven steady states, long time simulations (typically, longer than 50 000 a/c_s are necessary.

In Fig. 2, one can clearly identify the existence of two different regimes of confinement improvement (i.e., weak and strong) and of a power threshold to access to the strong ITB regime. This point is illustrated in the dotted lines in Fig. 2. Lines (i), (iii), and (iv) represent fitting curves for steady state ∇T_i for the L-mode case showing no confinement improvement, weakly, and strongly improved confinement regimes, respectively. Line (ii) denotes transitional ∇T_i just prior to the transition to the enhanced confinement regime. We calculated the L-mode case using a monotonic $q(r)$ profile, while keeping all other parameters identical to those in the reversed shear case. Given the limitation of the numerical model employed in this work (i.e., retaining only resonant modes), it is rather unclear if the transitions to enhanced confinement
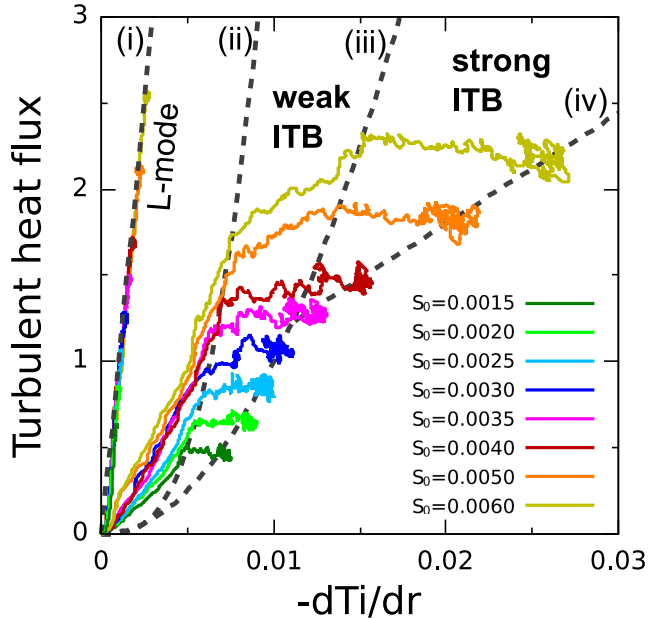
FIG. 2. Time trajectories for turbulent heat flux (Q_i) versus ion temperature gradient ($-\nabla T_i$) at ITB during TRB simulations. Time averages over $\Delta t = 2000$ (a/c_s) have been used. The steady-state temperature gradient at an ITB is determined by the power of a central heat source denoted by S_0. Dotted lines represent fitting curves for (i) the L-mode case showing no confinement improvement, (ii) the ITB formation points, and the steady-state temperature gradients at ITBs, when turbulence is (iii) weakly, and (iv) strongly suppressed, respectively. One can clearly identify two different regimes of confinement improvement (i.e., weak and strong) and of the power threshold to access to the strong ITB regime.

regimes shown in Fig. 2 correspond precisely to the formation of ITB. There are, however, some indications that this transition is likely to be consistent with the formation of ITBs, as demonstrated in Ref. 35. First, it involves positive feedback between the $E \times B$ shear ($\omega_{E \times B}$) and the formation of a steep ∇T_i. Second, it exhibits hysteresis when we perform power ramp up and down simulations.[35] It is on this basis that we designate steady states in lines (iii) and (iv) as weak and strong ITBs, respectively, in spite of the limitation of our numerical model.

Another way of parametrizing the degree of confinement improvement will be to use the Nusselt number, which is defined as the ratio of turbulent heat conductivity to the neo-classical one. In this paper, we use the time-averaged Nusselt number during a steady state, which is defined by

$$\langle \mathrm{Nu} \rangle \equiv \frac{1}{\chi_i^{neo}} \frac{1}{t_2 - t_1} \int_{t_1}^{t_2} \frac{Q_i^{\mathrm{turb}}}{-\nabla T_i} dt, \qquad (4)$$

where χ_i^{neo} is neoclassical ion thermal diffusivity, t_1 and t_2 are the start and the end time of a steady state, respectively, and Q_i^{turb} is turbulent heat flux. Figure 3 shows $\langle \mathrm{Nu} \rangle$ for various S_0 values shown in Fig. 2. As S_0 increases, $\langle \mathrm{Nu} \rangle$ decreases very rapidly and then saturates at $\langle \mathrm{Nu} \rangle \sim 3$, indicating strong suppression of turbulent transport. Hereafter, we use the high-Nusselt (high-Nu) and the low-Nusselt states (low-Nu) as synonymous with the weak and the strong ITBs, respectively, and vice versa, throughout this paper.

We note that $\langle \mathrm{Nu} \rangle$ in Fig. 3 is higher than unity in all cases. This implies that turbulent transport is still active even
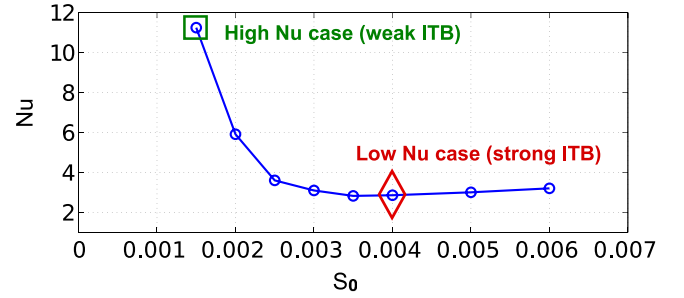

FIG. 3. Time-averaged Nusselt number ($\langle \mathrm{N}u \rangle$) during a stead-state versus the power of a heat source S_0. Here, $\langle \mathrm{Nu} \rangle = (1/\chi_i^{neo})[1/(t_1 - t_2)] \int_{t_1}^{t_2} (Q_i^{\mathrm{turb}}/\nabla T_i) dt$, where χ_i^{neo} is neoclassical ion thermal diffusivity, t_1 and t_2 are the start and the end time of a steady state under consideration, respectively, and Q_i^{turb} is turbulent heat flux. As S_0 increases, $\langle \mathrm{Nu} \rangle$ decreases very rapidly and then saturates at $\langle \mathrm{Nu} \rangle \sim 3$, indicating the strong suppression of turbulent transport. Two reference cases representing the high and the low $\langle \mathrm{N}u \rangle$ (i.e., the weak and the strong ITBs) are indicated in the figure.

in strong ITBs. We remark that $\langle \mathrm{Nu} \rangle$ for strong ion ITBs in this work is rather large as compared to actual experimental results. There $\langle \mathrm{Nu} \rangle \sim 1$ is characteristic of a strong barrier. This quantitative disparity is likely due to the limitations of this gyrofluid, TRB model. We remark that our studies of strong barriers with the Nusselt number greater than 1 may be directly relevant to the case of electron ITBs, however. We also remark that $\langle \mathrm{Nu} \rangle$ given in Eq. (4) includes heat flux coming from both diffusive and non-diffusive (avalanching, for instance) contributions.

Figure 2 also shows that stationary states with improved confinement are not completely quiescent. Noisy and/or relaxation-like transport events prevail in steady states, giving rise to the wobbling of ∇T_i. In fact, the main focus of this paper is to elucidate the origin of this noisy transport in steady high-Nu and low-Nu states where turbulent transport is reduced. To this end, we choose two reference cases: one represents a high-Nu ($\langle \mathrm{Nu} \rangle = 11.0$) state and the other stands for a low-Nu state ($\langle \mathrm{Nu} \rangle = 2.9$). They are indicated in Fig. 3.

Figures 4(a) and 4(b) show time-averaged profiles of ion temperature and $E \times B$ shear ($\omega_{E \times B}$), respectively, for the high-Nu (green dotted lines) and the low-Nu (red solid lines) states. In Fig. 4, we define an ITB by a shaded region and specify some important locations, such as the ITB shoulder ($r/a = \rho = 0.54$), the ITB center ($r/a = 0.58$), and the ITB foot ($r/a = 0.6$). The $E \times B$ shear profile in a steady state ITB shows a double hump structure, as can be seen in Fig. 4(b). The first hump, located at near the ITB shoulder position, is mainly due to the zonal flow contribution while the second hump, located at the ITB foot, comes mostly from the $\nabla V_{\parallel}$ contribution.[38] It will be shown later that these $\omega_{E \times B}$ peaks limit the propagation of a heat avalanche, especially in low-Nu states.

III. STATISTICAL ANALYSIS OF HEAT TRANSPORT

A. Heat flux probability density function

We begin our analysis by examining a PDF of heat flux. Right hand side of Figs. 5(a) and 5(b) shows heat flux PDFs at $r/a = 0.6$ for the reference high-Nu and low-Nu states, respectively. For comparison, we also present Gaussian fits
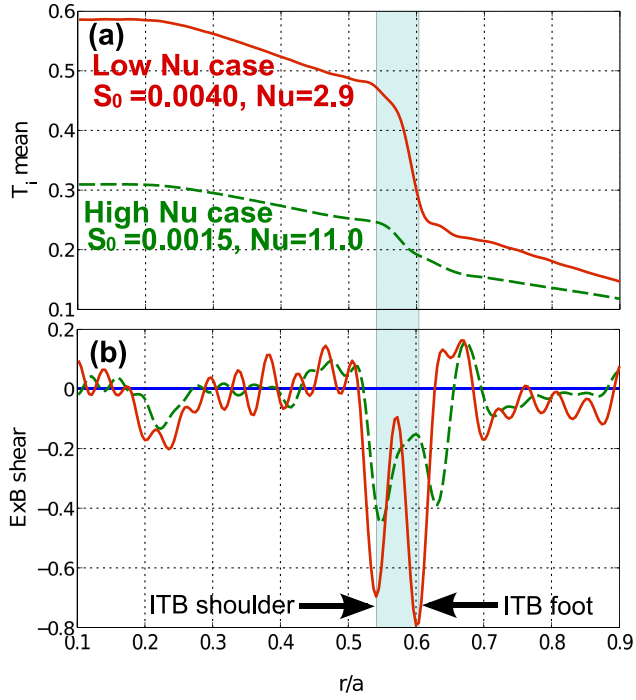
FIG. 4. Steady state radial profiles of (a) ion temperature and (b) the $E \times B$ shear for two reference cases indicated in Fig. 3. An ITB in this paper is defined by a steep gradient region (the shaded area) around the q_{min} position ($r/a = 0.6$). Two strong peaks of the $E \times B$ shear at the ITB shoulder ($r/a = 0.54$) and ITB foot ($r/a = 0.60$) sustain an ITB in a steady state.

to the heat flux PDFs. It is evident from the figures that the heat flux PDFs shows considerable deviation from Gaussian, especially for the low-Nu state. The peak of the Gaussian fit shifts to a higher value of heat flux due to the presence of "fat tails" in the original PDF. The degree of non-Gaussianity is usually quantified by the skewness (S) and kurtosis (K) parameters, which are the third and the fourth standardized moments of a random variable X, respectively,

$$ S = \frac{\int_{-\infty}^{\infty} (X - \mu)^3 P(X) dX}{\sigma^3}, \quad K = \frac{\int_{-\infty}^{\infty} (X - \mu)^4 P(X) dX}{\sigma^4}, $$

where μ is the mean value, σ the standard deviation, and $P(X)$ the probability density function. In this definition, S and K values for a Gaussian distribution are 0 and 3, respectively. We remark in passing that the usual definition of kurtosis involves –3 to make K of a Gaussian distribution equal to zero. S (K) values corresponding Figs. 5(a) and 5(b) are 0.51 (3.97) and 1.27 (5.71), respectively. This non-Gaussian feature of a heat flux PDF, in particular, the appearance of a fat tail suggests that heat avalanches play an important role in this regime.

The degree of non-Gaussianity varies with radius, as is shown in Figs. 6(a) and 6(b) where we plot S and K of the heat flux PDFs as a function of radius. Both S and K exhibit similar radial patterns. The deviation from a Gaussian PDF is most prominent at just inside the ITB foot of the low-Nu state, where K reaches up to ∼9. An interesting observation in Fig. 6 is that this radial pattern of non-Gaussianity parameters closely follows the $\omega_{E \times B}$ profile, shown in Fig. 4(b). Since we may interpret the degree of non-Gaussianity as the emergence of avalanching transport, this observation coincides with the hypothesis of formation of a meso-scale $E \times B$ flow pattern through the interaction with the spatial scale of heat avalanches.[18]

B. Frequency spectrum analysis

Having examined the non-Gaussian feature of the heat flux PDF in enhanced confinement regimes, we perform a spectral analysis of heat flux. Figures 7(a) and 7(b) show the PSDs of heat flux at the ITB center, $\rho = 0.58$, for the high-Nu and the low-Nu states, respectively. In calculating the power spectra, we used smoothed time series of heat flux that was
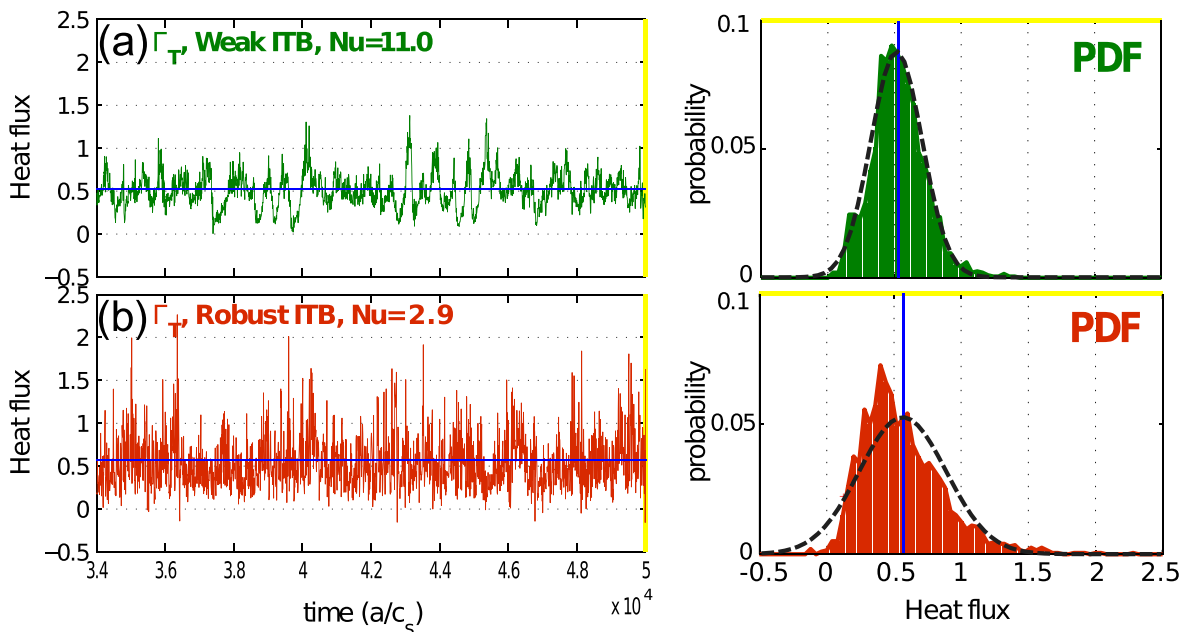

FIG. 5. Time series (left) and PDF (right) of heat flux at q_{min} position for the representative (a) high-Nu ($\langle Nu \rangle = 11.0$) and (b) low-Nu ($\langle Nu \rangle = 2.9$) states. The heat flux PDF in the low-Nu state shows a strong "fat tail" and significantly deviates from a Gaussian distribution, which is indicated by the dotted line.
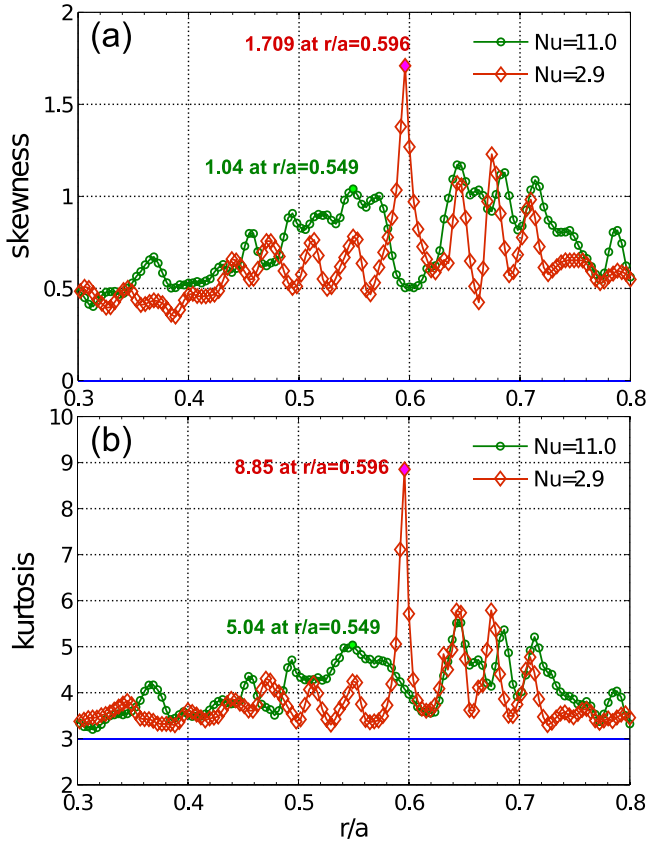
FIG. 6. Radial profiles of (a) skewness (S) and (b) kurtosis (K) of heat flux PDF for high-Nu (green) and low-Nu (red) states. S = 0 and K = 3 when a PDF is a Gaussian distribution. Both S and K exhibit similar patterns. Deviation from a Gaussian PDF is most prominent at just inside the ITB foot for the low-Nu state, where K rises to ~8.9. S and K profiles closely follow the $\omega_{E\times B}$ profile shown in Fig. 4(b).

obtained by averaging two adjacent sampling points. We also display slopes of f^{-1} (f: frequency) and f^{-2}. The power spectrum for the high-Nu state shows some marked peaks at low frequency around $1 \times 10^{-3} < fa/c_s < 2.5 \times 10^{-3}$, as can be seen in Fig. 7(a). In Sec. IV, it will be shown that these low frequency peaks in the heat flux represent quasi-periodic heat pulses, which are associated with the relaxation of the zonal flow at ITB shoulder.

Apart from the low frequency peaks, the overall power spectrum in high-Nu state shows mostly f^0 and f^{-2}

dependence, indicating the dominance of a diffusive transport process in this regime. To illustrate this point, we consider the autocorrelation function of heat flux, $\mathcal{R}^Q(\tau) = \int_{-\infty}^{\infty} Q(t) Q^*(t+\tau)dt$, where $Q^*(t)$ denotes the complex conjugate of $Q(t)$. Using the Wiener-Khinchin theorem, the power spectrum density, $|Q(\omega)|^2$, is given by the Fourier transform of $\mathcal{R}^Q(\tau)$,

$$|Q(\omega)|^2 = \int_{-\infty}^{\infty} \mathcal{R}^Q(\tau)e^{-i\omega\tau}d\tau. \tag{5}$$

Now, assume that heat transport is purely diffusive with an exponential autocorrelation function, $\mathcal{R}^Q(\tau) \sim e^{-\Delta\omega\tau}$, where $\Delta\omega$ is the inverse of turbulence decorrelation time. From a mixing length argument, $\Delta\omega \sim k^2 D$, where k is the maximum wavenumber and D is the turbulent diffusion coefficient. Then, Eq. (5) becomes

$$|Q(\omega)|^2 \sim \int_{-\infty}^{\infty} e^{-\Delta\omega\tau}e^{-i\omega\tau}d\tau = \frac{2k^2 D}{\omega^2 + (k^2 D)^2}. \tag{6}$$

It is easy to show that Eq. (6) yields ω^0 and ω^{-2} dependence of a PSD when $\omega \ll k^2 D$ (i.e., low frequency) and $\omega \gg k^2 D$ (i.e., high frequency), respectively. We thus conclude that the turbulent diffusion is still a dominant heat transport process in the high-Nu state, while non-diffusive heat transport is mostly due to the low frequency, quasi-periodic pulses.

Disappearance of a 1/f region of power spectrum when diffusive transport is dominant is also reported in Ref. 29 which studied heat transport based on a diffusive sandpile cellular automata model. In Ref. 29, ballistic, avalanching heat transport is still a dominant process even when diffusive transport is sufficiently large enough to extinguish the 1/f region. In contrast, however, diffusive transport is dominant in high-Nu state in the present work, and the non-diffusive transport takes the form of quasi-periodic heat pulses, rather than intermittent ballistic ones.

The power spectrum of the low-Nu state shows a marked contrast to that of the high-Nu state: the appearance of a broad 1/f region. This change of frequency spectrum implies a qualitative change in a transport process as ⟨Nu⟩ bceomes smaller. In fact, the 1/f frequency region in the
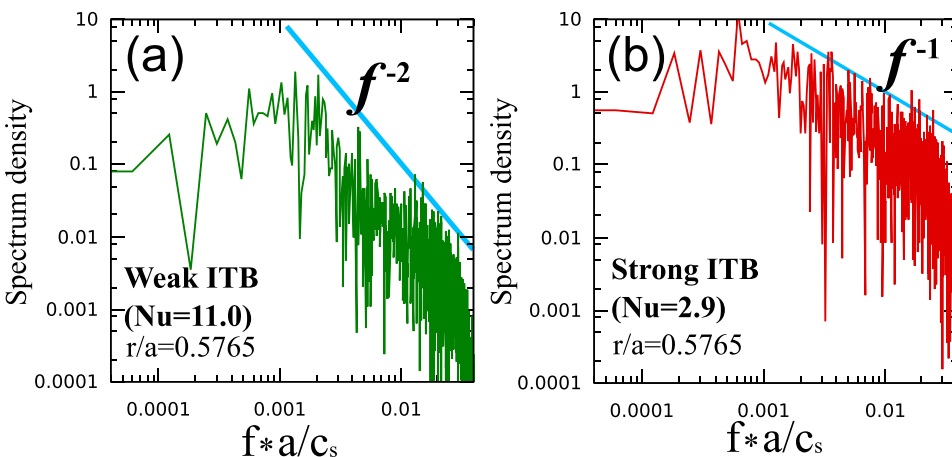

FIG. 7. PSDs of heat flux for (a) high-Nu and (b) low-Nu states at the ITB center position ($r/a = \rho = 0.5765$). ⟨Nu⟩ is indicated in the figures. The high-Nu state is characterized by the presence of marked quasi-periodic peaks around the $f = 1 \sim 2$ kHz region. The overall PSD in this case follows mostly f^0 and f^{-2} dependence, indicating the prevalence of diffusive heat transport. The PSD of heat flux for low-Nu state is characterized by the presence of a broad region of an avalanching 1/f power spectrum, as shown in (b).

power spectrum indicates the existence of SOC-like bursty, avalanching transport dynamics[22,25] when a strong transport barrier develops. A similar change of power spectrum has been reported when self-consistent zonal flows were included in the simulations of resistive ballooning turbulence in slab geometry.[31] The gradual appearance of the 1/f frequency region was also presented in Ref. 29 using a diffusive sandpile model including the possibility of suppression of diffusive transport, i.e., implying the formation of a strong transport barrier.

Of particular interest in this subsection is to quantify the ratio of transport heat avalanches to the total heat flux. Assuming that the episodic 1/f region of power spectrum is responsible for the production of most heat avalanches, it is possible to evaluate the heat flux coming from that frequency region. To this end, we calculate the cross power spectrum between the temperature and radial $E \times B$ fluctuations that is given by[39]

$$\mathcal{P}_{\tilde{T}\tilde{v}_r}(\mathbf{r}, \omega) = \mathcal{F}_{\tilde{T}}^*(\mathbf{r}, \omega)\mathcal{F}_{\tilde{v}_r}(\mathbf{r}, \omega),$$

where $\mathcal{F}_{\tilde{T}}(\mathbf{r}, \omega)$ and $\mathcal{F}_{\tilde{v}_r}(\mathbf{r}, \omega)$ denote the Fourier transform of $\tilde{T}(t)$ and $\tilde{v}_r(t)$, respectively. Then, it can be shown that the time averaged heat flux $\langle \tilde{v}_r(t)\tilde{T}(t) \rangle$ can be evaluated from this cross-power spectrum as

$$\langle \tilde{v}_r(\mathbf{r}, t)\tilde{T}(\mathbf{r}, t) \rangle = 2\mathrm{Re}\int_0^\infty \mathcal{P}_{\tilde{T}\tilde{v}_r}(\mathbf{r}, \omega)d\omega. \qquad (7)$$

Thus, one can interpret the cross power spectrum $\mathcal{P}_{\tilde{T}\tilde{v}_r}(\mathbf{r}, \omega)$ as a frequency-resolved heat flux density.

Figures 8(a) and 8(b) show $\mathcal{P}_{\tilde{T}\tilde{v}_r}(\omega)$ at $\rho = 0.6$ for the high-Nu and the low-Nu states, respectively. Using Eqs. (6) and (7), one can easily evaluate the heat flux coming from the quasi-periodic and the 1/f region of the power spectra. To do so, it is more convenient to use the linear frequency scale than the log scale employed in Figs. 8(a) and 8(b). Figure 8(c) shows $\mathcal{P}_{\tilde{T}\tilde{v}_r}(\omega)$ on a linear frequency scale and the cumulative power fraction of heat flux as a function of frequency that is defined by
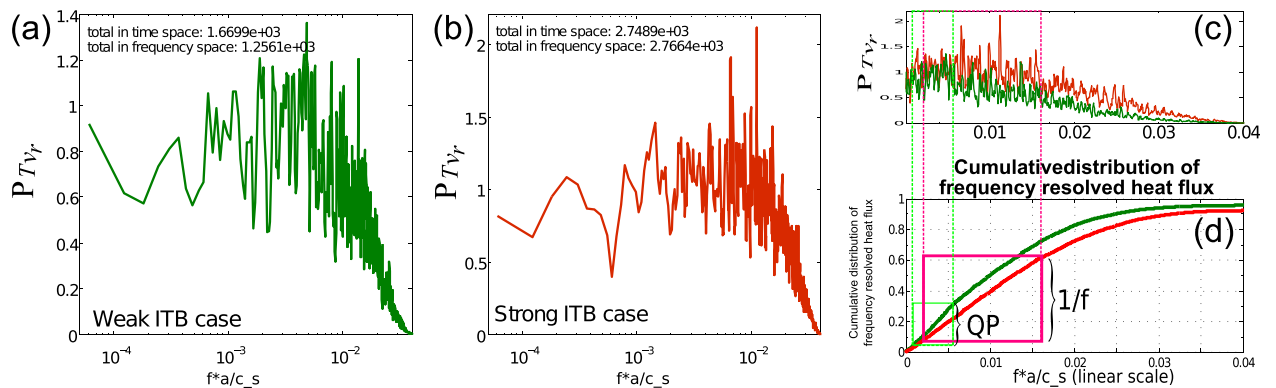
$$P_{cum}(\omega_0) = \frac{\displaystyle\int_0^{\omega_0} \mathcal{P}_{\tilde{T}\tilde{v}_r}(\omega)d\omega}{\displaystyle\int_0^{\infty} \mathcal{P}_{\tilde{T}\tilde{v}_r}(\omega)d\omega}.$$

In Fig. 8(c), the green and red lines denote the high-Nu and the low-Nu states, respectively. Also, boxes in Fig. 8(d) indicate approximate ranges of quasi-periodic (green) and 1/f (red) frequency regions estimated from the power spectra. Then, it is easy to assess the amount of non-diffusive heat transport. For the high-Nu state, ~20 % of heat flux comes from the quasi-periodic oscillations, while episodic 1/f avalanching heat transport takes up about ~50 % of the total heat transport for the low-Nu state. Thus, we conclude that avalanching heat transport becomes a dominant process when a barrier becomes stronger. This result suggests that qualitatively different dynamics may govern heat transport in a well-developed barrier, where turbulent transport is strongly suppressed. For instance, our results may indicate the dominance of avalanching heat transport in edge localized mode (ELM)-free H-mode plasmas, even in the absence of MHD instabilities.

IV. CHARACTERISTICS OF HEAT AVALANCHES

In Sec. III, we showed that two different avalanching heat transport processes pertain to improved confinement regimes, depending on their strength. When turbulence is weakly suppressed (i.e., high-Nu state), heat avalanches take the form of low frequency QP oscillations or pulses, which manifest themselves as distinct peaks in a power spectrum density. As Nusselt number becomes smaller, these QP heat pulses disappear and bursty heat avalanches characterized by the presence of a 1/f frequency region, emerge as the dominant heat transport process. In this section, we study the detailed characteristics of these heat avalanches in improved confinement regimes, based on a statistical spatio-temporal correlation analysis.

A. Quasi-periodic heat pulses: High-Nu state

Figure 9(a) shows a contour plot of the two-point correlation coefficient of heat flux $\mathcal{C}_{\rho_a}^Q$, which is defined by

FIG. 8. Frequency-resolved heat flux (i.e., the cross-power spectra between $\tilde{T}$ and $\tilde{v}_r$) for (a) high-Nu and (b) low-Nu states in logarithmic scale. Cumulative power fraction of heat flux for the two reference cases are presented in (d) along with the frequency-resolved heat fluxes shown for linear scales in (c). Green and red lines in (c) and (d) denote the high-Nu and the low-Nu states, respectively. Heat flux values at the ITB foot position ($r/a = 0.6$) have been used. Contributions to the heat flux from low frequency quasi-periodic oscillations in the high-Nu state (i.e., weak ITB), and the 1/f region for the low-Nu state (i.e., strong ITB) are estimated to be ~20% and ~50% of the total heat flux, respectively.
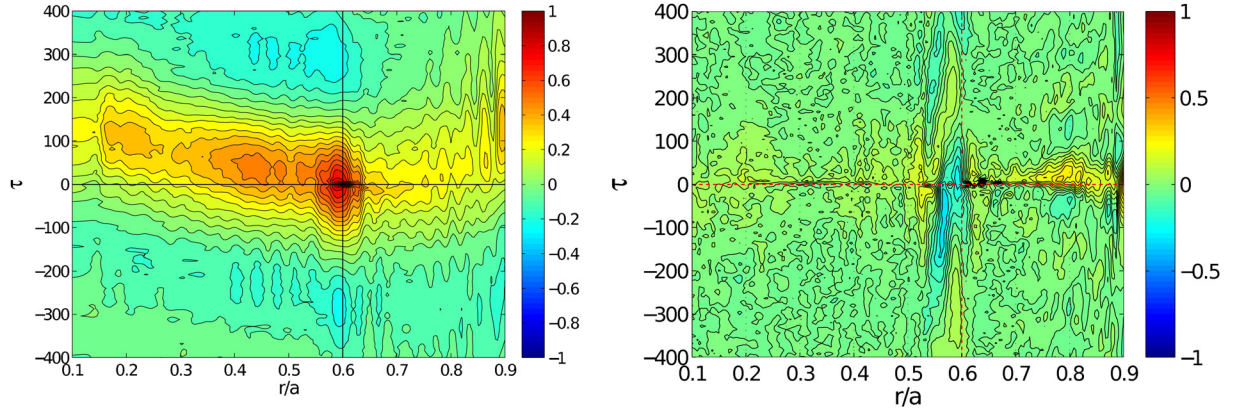
FIG. 9. Contour plots of the cross-correlation (a) of heat flux between $r/a = \rho = 0.6$ (the position of q_{min}) and other spatial locations and (b) between heat flux and $E \times B$ shearing rate ($\omega_{E \times B}$) in the representative high-Nu state with $\langle \mathrm{Nu} \rangle = 11.0$. A heat pulse, initiated from the ITB shoulder ($r/a = 0.54$) and progating both inward and outward, produces a long-range correlation covering almost an entire system size. The strong anti-correlation at the ITB shoulder position ($r/a = \rho_1$) with the time lag $\tau \sim -100$ indicates that the degradation of $\omega_{E \times B}$ happens at there prior to the generation of a heat pulse, suggesting a sudden drop of $\omega_{E \times B}$ at $\rho = \rho_1$ is responsible for triggering of heat pulses in the high-Nu state.

$$\mathcal{C}^Q_{\rho_a}(\rho, \tau) \equiv \mathcal{R}^Q_{\rho_a}(\rho, \tau)/\mathcal{R}^Q_{\rho_a}(\rho_a, 0), \qquad (8)$$

with $\mathcal{R}^Q_{\rho_a}(\rho, \tau) = \int Q(\rho, t) Q^*(\rho_a, t + \tau) dt$, where $Q(\rho, t)$ is the heat flux at $\rho = r/a$, τ the time lag, and the time integration in $\mathcal{R}^Q_{\rho_a}(\rho, \tau)$ is taken over the duration of a steady state. In Fig. 9, we take $\rho_a = 0.6$, which is the position of q_{min} ($\rho_{q_{min}}$). Figure 9(a) represents the cross-correlation between the heat flux at $\rho_{q_{min}}$ and other spatial locations. One can easily identify a prominent, long-range correlation produced by a heat pulse. The heat pulse is initiated at the ITB shoulder and propagates both inward and outward. The radial extent of the two-point correlation spans almost an entire system size.

The inward propagation speed of a heat pulse is a little faster than that of outward propagation. The propagation speed of a QP pulse is estimated to be $v_g \sim 4 \times 10^{-3} c_s$ and $v_g \sim 3 \times 10^{-3} c_s$ for inward and outward propagation, respectively. This propagation speed falls within a range of $\epsilon \rho^* \leq v_g/c_s \leq \rho^*$, where ϵ is the inverse aspect ratio, although this scaling is uncertain in this work, due to the lack of ρ^* scan. Recent full-f gyrokinetic simulations report that v_g follows the scaling $v_g \sim v_*$ (v_*: diamagnetic drift velocity) or $v_g \sim \rho_i c_s/R$,[15–17] which seem to agree with our observation. The retardation of an outward pulse is due to the presence of strong $\omega_{E \times B}$ at ITB foot position, as indicated in Fig. 9(a). It acts like a hurdle hindering a heat pulse from propagating outward. Retardation of a heat pulse (or a heat avalanche) by $\omega_{E \times B}$ was also observed in recent simulations.[40]

Figure 10 shows spatio-temporal evolution of the perturbed ion temperature $\delta T_i(r, t) = T_i(r, t) - \langle T_i(r, t) \rangle$, where $\langle T_i(r, t) \rangle$ is the time-averaged temperature during a steady state in the high-Nu state. It indicates that a QP pulse causes simultaneous inward propagation of a *void* (i.e., negative δT_i) and outward propagation of *bump* (i.e., positive δT_i) in the temperature profile.

A natural question is then what the physical origin of the QP heat pulses is in high-Nu states. To answer this question, we evaluate the cross-correlation coefficients between heat flux and $\omega_{E \times B}$ in a similar manner to Eq. (8),

$$\mathcal{C}^Q_{\omega_{E \times B}}(\rho, \tau) \equiv \mathcal{R}^Q_{\omega_{E \times B}}(\rho, \tau)/\mathcal{R}^Q_{\omega_{E \times B}}(\rho, 0), \qquad (9)$$

with $\mathcal{R}^Q_{\omega_{E \times B}}(\rho, \tau) = \int Q^*(\rho, t)|\omega_{E \times B}(\rho_a, t + \tau)|dt$, where the time integration is taken over the duration of a steady state. Figure 9(b) represents a contour plot of $\mathcal{C}^Q_{\omega_{E \times B}}(\rho, \tau)$ evaluated from Eq. (9). One can see from Fig. 9(b) a clear anti-correlation between heat flux and $|\omega_{E \times B}|$ (shown in blue color) at the ITB shoulder position, $\rho = 0.54 \equiv \rho_1$, which correspond to the position of the first $\omega_{E \times B}$ peak in Fig. 4(b), with the time lag, $\tau \sim -100$. It suggests that a drop of $\omega_{E \times B}$ at $\rho = \rho_1$ is responsible for the triggering of the QP heat pulse. This interesting finding is reinforced by Fig. 11 where the power spectrum of $\omega_{E \times B}$ at $\rho = \rho_1$ is depicted. It is easy to show that low frequency peaks in Fig. 11 (centered at $f \sim 1$ kHz) well coincide with those in the power spectrum of heat flux, Fig. 7(b). This implies a strong correlation between relaxation oscillations in $\omega_{E \times B}$ at $\rho = \rho_1$ and the generation of QP heat pulses in the high-Nu state.

Once generated, a heat pulse propagates without clear correlation with $\omega_{E \times B}$. A heat pulse then pump out heat out of the enhanced confinement region in the form of a temperature profile bump, as shown in Fig. 10. Note that the profile
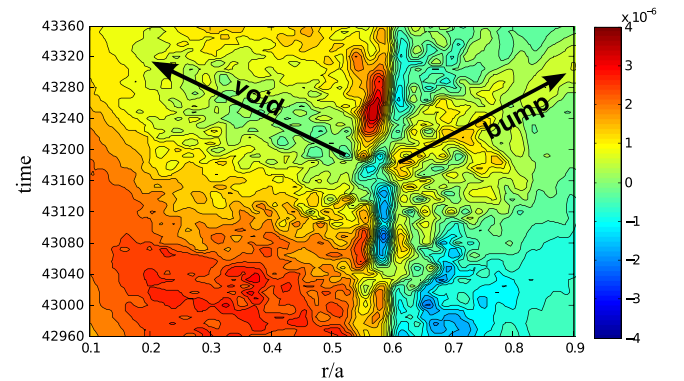

FIG. 10. Spatio-temporal evolution of the perturbed ion temperature, $\delta T_i(r, t) = T_i(r, t) - \langle T_i(r, t) \rangle$, where $\langle T_i(r, t) \rangle$ is the time-averaged temperature during a steady state, in the stationary high-Nu state. A quasi-periodic heat pulse causes simultaneous inward propagation of a *void* (i.e., negative δT_i) and outward propagation of *bump* (i.e., positive δT_i) in the temperature profile, effectively pumping heat out of the core region.
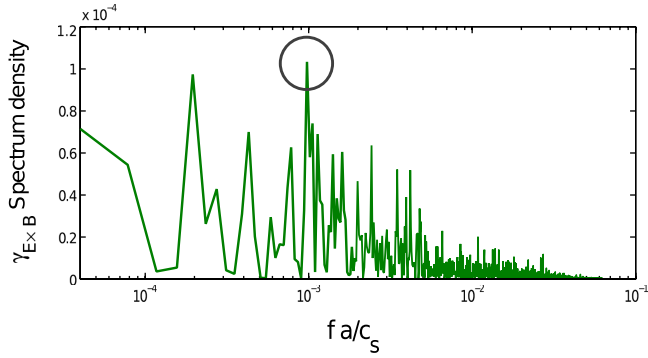
FIG. 11. PSD of the $E \times B$ shearing rate ($\omega_{E \times B}$) at the ITB shoulder position, showing a strong peak at approximately the same frequency region as in the PSD of heat flux shown in Fig. 7(a). The representative high-Nu state with $\langle \mathrm{N}u \rangle = 11.0$ has been used.

bump propagates outward while the profile void propagates inward, thus effectively removing heat from the core region. In this sense, $\omega_{E \times B}$ at the ITB shoulder functions like a *heat valve*, pulling heat out of the plasma core region.

Since $\omega_{E \times B}$ at $\rho = \rho_1$ is mostly due to the zonal flow as described in Sec. II B, it is quite natural to suspect that the peaks shown in Fig. 11 originate from the collisional relaxation of the zonal flow.[41,42] This possibility can be studied by repeating simulations with varying numerical values of prescribed neoclassical viscosity (μ_{neo}). Figure 12(a) shows power spectra of $\omega_{E \times B}$ at the ITB foot for three different values of μ_{neo}. The middle row corresponds to the reference case shown in Fig. 11. It is obvious from the figure that the peak frequency increases as μ_{neo} increases. Simultaneously, low frequency peaks of the heat flux power spectrum also increase accordingly, which demonstrates a strong correlation between the QP heat pulses and the collisional relaxation oscillations of the zonal flow at the ITB shoulder. Figure 12(b) shows the autocorrelation coefficient $\mathcal{C}^Q(\tau)$ of heat flux at the ITB foot position for three values of μ_{neo} being used to produce Fig. 12(a). As μ_{neo} increases, the period of $\mathcal{C}(\tau)$ decreases implying more frequent bursts of heat pulses. In this figure, negative values of $\mathcal{C}(\tau)$ after some time lag represent an anti-correlation and signify the quasi-periodic nature of the time-series data shown in Fig. 5(a). This provides further evidence for zonal flow-QP heat pulse correlation.

Existence of quasi-periodic heat pulses in high-Nu states due to the relaxations of zonal flow has an interesting similarity to recent experiments. Kim and Diamond first predicted the possibility of transient oscillations of a transport barrier prior to barrier formation owing to the competition between zonal flow and turbulence.[41] The existence of this transient oscillatory period, the dithering phase or I-phase, has been recently observed prior to the transition to H-modes at DIII-D[43] and TJ-II,[44] and during L-H transition with marginal threshold power at EAST.[45] All of these observations involve the formation of a weak barrier (I-phase is a weak barrier). Thus, these findings strongly suggest that QP transport events due to the zonal flow relaxation are ubiquitous phenomena when a weak transport barrier forms. In fact, such QP oscillations that are strongly correlated with $\omega_{E \times B}$ at the barrier, disappear in the low-Nu states, as will be shown in Subsection IV B.
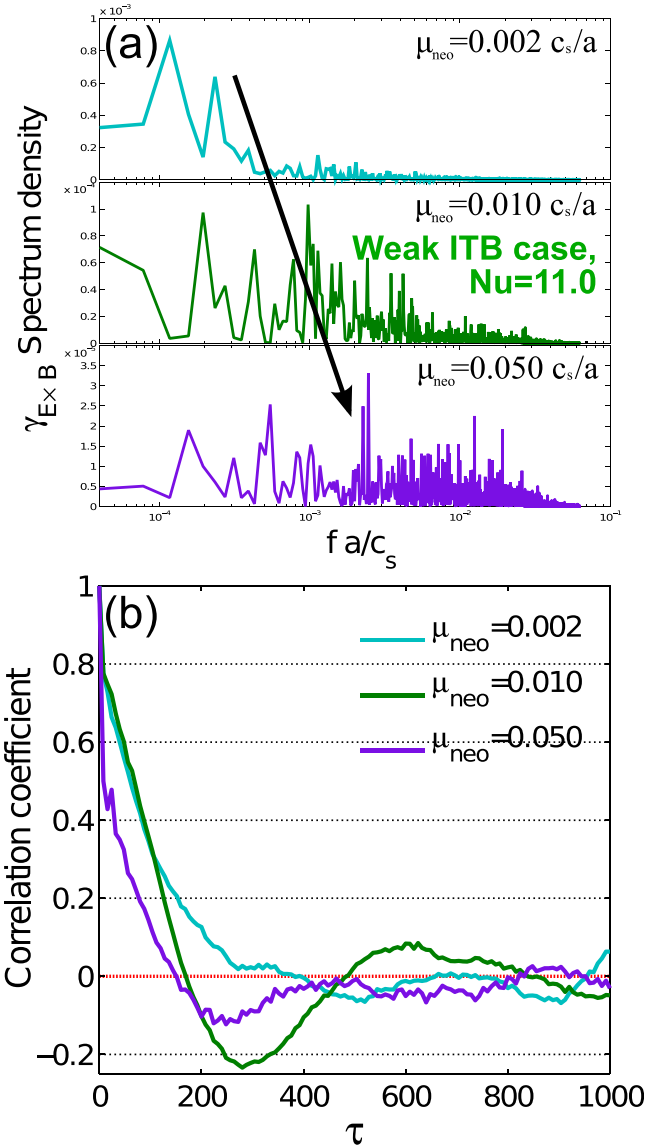

FIG. 12. (a) Change of PSD of $\omega_{E \times B}$ at the ITB shoulder position ($r/a = \rho = \rho_1$) when three different values of the prescribed neoclassical viscosity (μ_{neo}) are used. The middle row corresponds to the reference high-Nu state shown in Fig. 11. As μ_{neo} increases, the peak frequency of $\omega_{E \times B}$ PSD increases, indicating that quasi-periodic heat pulses come from the collisional relaxations of zonal flow at the ITB shoulder. (b) Autocorrelation coefficient ($C(\tau)$) of heat flux at $\rho = \rho_1$ for three different values of μ_{neo} being used in (a). As μ_{neo} increases, the period of $C(\tau)$ decreases implying more frequent bursts of heat.

B. Episodic 1/f heat avalanches: Low-Nu state

Figure 13(a) shows a contour plot of the two-point correlation coefficient of heat flux ($\mathcal{C}^Q_{\rho_a}$), which is defined by Eq. (9) with $\rho_a = 0.6$. Basically, this plot is the counterpart of Fig. 9(a) in the low-Nu state. One can recognize the absence of a prominent long-range correlation, in contrast to the high-Nu state where the correlation length almost spans an entire system size. The strong $\omega_{E \times B}$ at ITB shoulder prevents a heat avalanche from propagating into the core region. Thus, the shear at the zonal flow shoulder effectively decouples the core region from the ITB and the region beyond of it. Another difference is the lack of cross-correlation between heat flux and $\omega_{E \times B}$ at $\rho = \rho_1$, as illustrated in Fig. 13(b),
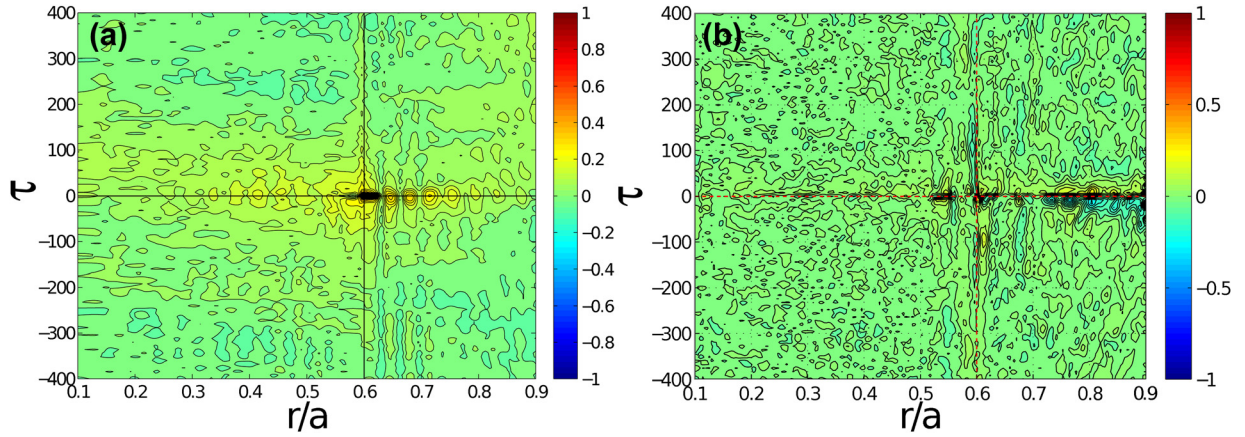
FIG. 13. Contour plots of the cross-correlation (a) of heat flux between $r/a = \rho = 0.6$ (the position of q_{min}) and other spatial locations and (b) between heat flux and $E \times B$ shearing rate ($\omega_{E \times B}$) at the ITB shoulder ($\rho = \rho_1$) in the reference low-Nu state with $\langle Nu \rangle = 2.9$. In contrast to the high-Nu state shown in Fig. 9, the long-range correlation of heat flux disappears and avalanching heat transport shows no clear correlation with the $\omega_{E \times B}$ at $\rho = \rho_1$.

where a contour plot of the cross-correlation between them is plotted. Thus, the triggering of 1/f heat avalanches in the low-Nu state is not directly related to the $E \times B$ shearing at the ITB shoulder.

To study the influence of $\langle Nu \rangle$ on the correlation length of a heat pulse/avalanche, we evaluate the two-point correlations of heat flux as a function of input power, the result of which is shown in Fig. 14. We take the ITB center position as the reference position in calculating the two-point correlations. The two locations of $\omega_{E \times B}$ peaks are indicated by two black dashed lines in Fig. 14. In producing Fig. 14, we took the maximum value of two-point correlation coefficients over time lag τ to designate a correlation coefficient at some radial position. Figure 14 shows a drop in the correlation length, defined by a e-folding length of the correlation coefficients between two points, as $\langle Nu \rangle$ becomes smaller. In low-Nu states, a robust $\omega_{E \times B}$ peak at the ITB shoulder prevents heat avalanches from propagating inward to the core region. Exactly, the same tendency is observed when we evaluate

correlation coefficients of heat flux by taking the ITB shoulder position as a reference: the strong $\omega_{E \times B}$ at the ITB foot blocks outward heat avalanches (not shown). Thus, the narrow enhanced confinement layer acts like an insulator, effectively trapping avalanches within it. In this circumstance, the heat avalanche proximity to the second peak of $\omega_{E \times B}$ is responsible for disposal of accumulated heat outside the barrier, to maintain a steady state.

The existence of a 1/f frequency band in the power spectrum density implies a self-similar temporal behavior of heat flux. This can be easily checked by exploiting, again, the Wiener-Khinchin theorem, $\mathcal{R}_Q(\tau) = \mathcal{F}^{-1}(\mathcal{S}_Q(f)) = \mathcal{F}^{-1}(1/f)$. Here, $\mathcal{R}_Q(\tau)$ is the autocorrelation function, $\mathcal{F}^{-1}$ is the inverse Fourier transform, $\mathcal{S}_Q(f)$ is the power spectrum, and $\mathcal{S}_Q(f) \propto 1/f$ is assumed. Then, the scaled autocorrelation function is given by

$$\mathcal{R}_f(\alpha\tau) = \mathcal{F}^{-1}\left(\frac{1}{\alpha}\mathcal{S}_f(f/\alpha)\right) = \mathcal{F}^{-1}\left(\frac{1}{\alpha} \cdot \frac{\alpha}{f}\right)$$
$$= \mathcal{F}^{-1}(1/f) = \mathcal{R}_f(\tau).$$

Power law autocorrelation functions of the form $\mathcal{R} \propto \tau^{-\beta}$ are self-similar. A power law autocorrelation thus signifies the existence of long temporal correlation. Figure 15(a) shows autocorrelation coefficients of heat flux in the reference low-Nu state. The blue shaded region in this figure indicates the range of time lag ($66.6 \lesssim \tau \lesssim 500$ in the units of a/c_s) corresponding to the 1/f frequency band ($2 \times 10^{-3} \lesssim f \lesssim 1.5 \times 10^{-2}$ in the units of c_s/a) in the power spectrum. It shows the power law decay of autocorrelation ($\mathcal{R} \sim \tau^{-1.6}$) in the blue shaded region, implying the existence of a long temporal correlation of episodic heat avalanches.

The presence of a long temporal correlation can also be studied by calculating the Hurst exponent, which is a well-known measure of self-similarity.[46–48] Actually, the Hurst exponent is not always relevant to the long temporal correlation but basically related to the temporal scaling of events.[49] To evaluate the Hurst exponent (H), we employ the method of rescaled range analysis.[50] In this approach, H is evaluated by power law fitting
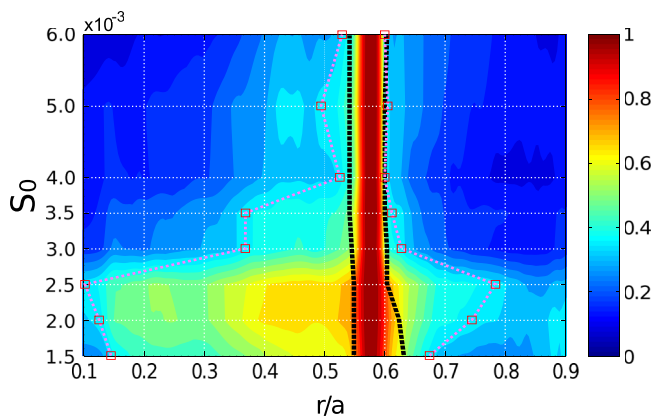

FIG. 14. Two-point correlation of heat flux between the ITB center and other spatial locations as a function of the power of a heat source (S_0). Locations of two $\omega_{E \times B}$ peaks shown in Fig. 4(b) are indicated by two black dashed lines. The correlation length shrinks significantly as power increases (i.e., $\langle Nu \rangle$ decreases). In the low-Nu regime, the robust $\omega_{E \times B}$ peak at the ITB shoulder prevents heat avalanches from propagating inward. In this sense, the narrow enhanced confinement layer plays a role of insulator, effectively confining avalanches therein.
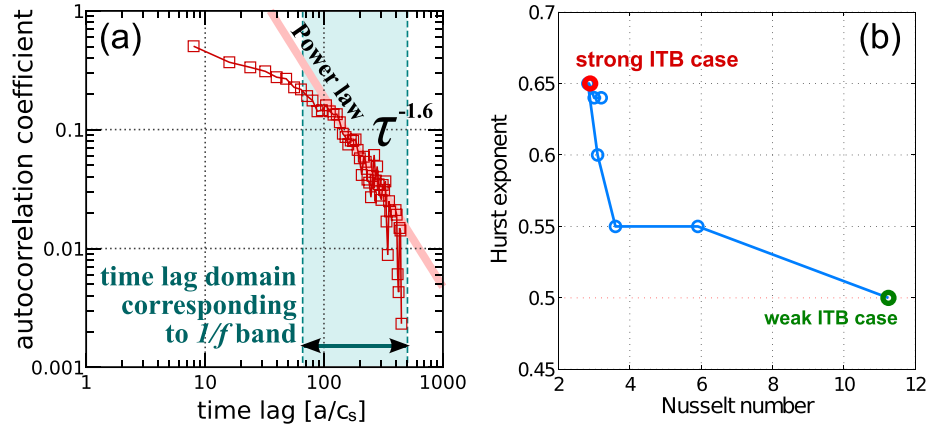
FIG. 15. (a) Autocorrelation coefficients of heat flux ($\mathcal{R}(\tau)$) at the position of q_{min} for the reference low-Nu state. Blue shaded region indicates the range of time lag $66.6a/c_s \lesssim \tau \lesssim 500a/c_s$ corresponding to the 1/f frequency band, $2 \times 10^{-3}c_s/a \lesssim f \lesssim 1.5 \times 10^{-2}c_s/a$. One can clearly observe the power law decay of autocorrelation ($\mathcal{R}(\tau) \sim \tau^{-1.6}$) in the shaded region, indicating of the existence of a long temporal correlation of the heat avalanches. (b) Hurst exponent (H) defined by Eq. (10) as a function of $\langle Nu \rangle$. The time series data of averaged heat flux over the ITB region ($0.54 \lesssim r/a \lesssim 0.60$) are used to calculate H. As $\langle Nu \rangle$ decreases, H becomes larger than 0.5, which signifies the emergence of long time correlation. H saturates at $H \sim 0.65$.

$$E[R(n)/S(n)] \rightarrow \lambda n^H, \qquad (10)$$

when the total number of time-series data under consideration, n, is sufficiently large. In Eq. (10), $E[\xi]$ denotes an expectation value of ξ, $R(n)/S(n)$ is the rescaled range, $R(n) \equiv \max(0, W_1, W_2, \ldots, W_n) - \min(0, W_1, W_2, \ldots, W_n)$ is a series of the maximal range of W_k, $W_k \equiv \sum_{j=1}^{k} Y_j$ with $Y_j = X_j - \mu$, μ is mean value, and $S(n)^2 \equiv \frac{1}{n}\sum_{j=1}^{n} Y_j^2$ is the standard deviation. A value H in the range $0.5 < H < 1$ $(0 < H < 0.5)$ indicates a time series with long positive temporal autocorrelation (anti-correlation). $H = 1/2$ implies that the series data under consideration is completely uncorrelated (i.e., random).

Figure 15(b) shows the Hurst exponent as a function of $\langle Nu \rangle$. We used time series data of heat flux averaged over an

enhanced confinement region ($0.54 \leq r/a \leq 0.60$) to calculate H. It shows the increase of H beyond 0.5 as the input power increases, signifying the emergence of long time correlation when $\langle Nu \rangle$ is small, consistent with Fig. 15(a). The Hurst exponent does not grow continuously but saturates at $H \sim 0.65$.

We sometime refer to heat avalanches with a 1/f power spectrum as SOC-like avalanching transport. A conventional SOC system presumes the presence of a random external source. In a sandpile model, for instance, it corresponds to the random grain deposition. Then, the probability of generating an avalanche follows a Poisson distribution. In this case, the probability distribution of the time interval between two successive avalanches, the QTD, is given by an exponential distribution, $P(\tau_q) \propto \exp[-\lambda\tau_q]$,[51] where τ_q is the time interval between the successive bursts (quiet time) and λ is a parameter. So, it is of interest to evaluate QTD of heat flux in the low-Nu state without any external random source to study if it is consistent with a standard SOC model.

To evaluate a QTD, we use the threshold method[51,52] in which the quiet time and the duration of an avalanche is defined with respect to a prescribed threshold value of heat flux. Figure 16 shows a QTD of the time series data given in Fig. 5(b) using the mean heat flux as the threshold value. It shows that the best fit for the QTD is a power law, implying the existence of correlation among avalanches. We note that the observation of a power law QTD in the low-Nu state agrees with the result reported in Ref. 27 in the context of a bistable sandpile model. In Ref. 27, a QTD begins to deviate from an exponential distribution, as the deposition rate of sand grains increases. This is, in some sense, equivalent to the increase of heat flux in our case. This suggests a rationale explaining the use of a simple running sandpile model to study qualitative characteristics of heat transport in the presence of transport barriers.
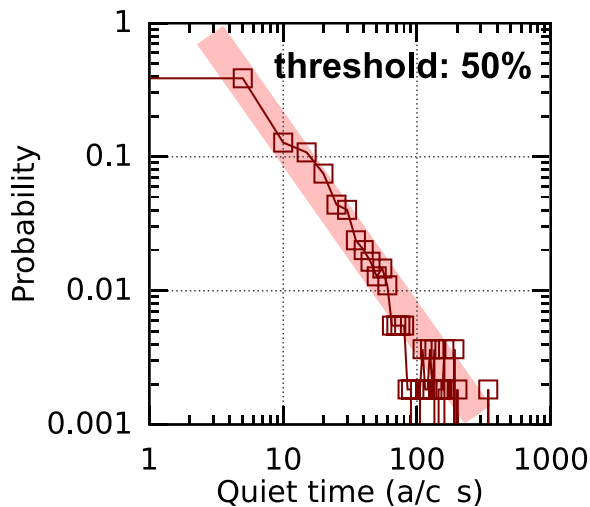

FIG. 16. QTD of heat flux at the position of q_{min} for the reference low-Nu state. Time series data given in Fig. 5(b) have been used. We use the threshold method[51,52] where the mean heat flux is set as a prescribed threshold value. One can observe a power-law distribution, implying the existence of correlation among avalanches in contrast to standard SOC phenomena. The appearance of a power-law QTD in the enhanced confinement regime agrees with Ref. 27, which evaluates QTD in the context of a bistable sandpile model.

V. SUMMARY AND CONCLUSIONS

In conclusion, this paper presented a statistical analysis of heat transport in stationary, flux-driven enhanced

confinement states. We used the time-averaged Nusselt number, $\langle Nu \rangle$, as a measure of improved confinement. We have focused on how the characteristics of non-diffusive avalanching heat transport vary as $\langle Nu \rangle$ changes. Long-time gyrofluid simulations with electrostatic ITG turbulence were performed to obtain flux-driven steady states with a statistically meaningful amount of time series data. In our simulations, $V_{\|}$ and T_i profiles evolve self-consistently in the presence of ITG turbulence, while profiles of safety factor, plasma density, and electron temperature are fixed in time.

After observing considerable deviation of the heat flux PDFs from a Gaussian, we performed a spectral analysis. In particular, we calculated the frequency-resolved heat flux in an attempt to quantify the amount of heat flux coming from heat avalanches, as opposed to the diffusive component. Finally, a spatio-temporal correlation analysis was carried out to identify characteristics of heat avalanches in high-Nu and low-Nu states. The main results of this paper are summarized as follows:

(1) A significant fraction of heat transport in stationary improved confinement regimes comes from non-diffusive heat avalanches, ranging from 20% to 50%, depending on the degree of turbulence suppression. The characteristics of avalanching heat transport change when turbulence is strongly suppressed (i.e., when $\langle Nu \rangle$ decreases).

(2) In high-Nu states, heat avalanches take the form of quasi- periodic (QP) heat pulses. These QP heat pulses are associated with collisional relaxation of the zonal flow at ITB shoulder, where the zonal flow contribution to $E \times B$ shear is maximal. The $E \times B$ shear at ITB shoulder functions like a *heat valve*, allowing the passage of heat from the plasma core. A QP pulse has a long spatial correlation, covering an entire system size and propagates in the inward and outward directions.

(3) In low-Nu states, episodic heat avalanches with a 1/f frequency band in heat flux power spectrum become the dominant transport process. Temporal correlation analyses show that heat avalanches have long temporal correlation. This conclusion is reinforced by a quiet time probability analysis. A heat avalanche is confined to a region between two strong $E \times B$ peaks, as occurs in the $E \times B$ staircase.[18]

In Sec. IV A, we pointed out the interesting similarity between the phenomena of QP heat pulses and transient dithering (or limit cycle oscillations) of a transport barrier observed in recent experiments.[43–45] Both involve the formation of relatively weak barriers near the threshold heat flux. This suggests that the QP heat pulses is likely to be ubiquitous phenomenon when a weak barrier forms. The fact that the QP pulses are likely to originate from the relaxation oscillations of zonal flow at the ITB shoulder due to collisional damping and the competition with background turbulence, as shown in Fig. 12(a), has an interesting implication. It suggests that more frequent QP heat pulses will be generated if collisionality increases. This suggests a possible interpretation for the mitigation of ELMs by supersonic molecular beam injection (SMBI) in HL-2A and KSTAR

devices:[53] namely, by generation of more frequent smaller heat pulses by SMBI due to the increase of collisionality.

Our results also suggest that heat transport is still present in a well-developed improved confinement regime, in the form of episodic heat avalanches. So, we predict that avalanching heat transport may be persistent, for instance, in ELM-free H-mode or quiescent H-mode (QH mode) plasmas. The fraction of heat transported by heat avalanches may then be obtained from the frequency-resolved heat flux as proposed in this paper.

The observed persistence of nonlocal heat avalanches in strong barriers raises the question of the applicability mean field theory (i.e., quasi-linear theory) for the study of transport through barriers. Our results suggest that it is necessary to study the fully nonlinear stochastic dynamics to understand transport in strong transport barriers. In particular, we note that, paradoxically, the flux PDF is strongly non-Gaussian, in spite of the fact that the turbulence is weak ($\langle Nu \rangle \sim 2$). This paradox challenges to the conventional wisdom.

An interesting question is how the characteristics of the episodic 1/f heat avalanches vary when a system size changes (i.e., ρ^* scan). Obviously, this will be of particular interest in predicting the energy confinement scaling of an ITER steady state plasma with an ITB. Hence, the questions like (1) how the fraction of avalanching transport (i.e., the ratio between diffusive and avalanching heat transport) changes with ρ^*, and (2) how the heat diffusivity scales with ρ^* [in other words, how the parameter α defined by $\chi_i = \chi_{Bohm}\rho^{*\alpha}$, where χ_i (χ_{Bohm}) is the turbulent (Bohm) heat diffusivity, changes with ρ^* in strong barriers], are of both fundamental and practical interest. Ultimately, we hope to understand the link between the ratio in (1) and the exponent α in (2).

Another important conclusion of this work follows from its relevance to nonlocality phenomena. In particular, the finding that avalanches exhibit long correlation lengths suggests a natural explanation for nonlocal heat transport, observed in the studies of response to localized perturbations.[54,55]

Heat transport in ITBs is related to momentum transport, as elucidated in recent experimental[56] and simulation[35,57] studies. Recent gyrokinetic simulations also show the close connection between heat and momentum avalanches in L-mode, showing cross PDFs by which outward heat avalanches induce inward momentum avalanches.[57] In particular, a recent study highlights the important role of momentum redistribution by Reynolds stress bursts in the formation and back transition of an improved confinement regime.[58] Non-Gaussianity of a Reynolds stress (momentum flux PDF) has also been discovered in an experimental study.[59] Establishing the relationship between heat and momentum PDFs or cross-PDF in momentum barriers, dominated by either intrinsic rotation or externally driven flow, is an interesting subject and will be reported in the future.

ACKNOWLEDGMENTS

[1]X. Litaudon, Plasma Phys. Controlled Fusion **48**, A1 (2006).

[2]R. C. Wolf, Plasma Phys. Controlled Fusion **45**, R1 (2003).

[3]F. Wagner, Plasma Phys. Controlled Fusion **49**, B1 (2007).

[4]A. E. Hubbard, Plasma Phys. Controlled Fusion **42**, A15 (2000).

[5]H. Biglari, P. H. Diamond, and P. W. Terry, Phys. Fluids B **2**, 1 (1990).

[6]T. S. Hahm and K. H. Burrell, Phys. Plasmas **2**, 1648 (1995).

[7]P. A. Politzer, Phys. Rev. Lett. **84**, 1192 (2000).

[8]P. A. Politzer, M. E. Austin, M. Gilmore, G. R. McKee, T. L. Rhodes, C. X. Yu, E. J. Doyle, T. E. Evans, and R. A. Moyere, Phys. Plasmas **9**, 1962 (2002).

[9]B. P. van Milligen, E. de la Luna, F. L. Tabarés, E. Ascasíbar, T. Estrada, F. Castejón, J. Castellano, I. García-Cortés, J. Herranz, C. Hidalgo, J. A. Jimenez, F. Medina, M. Ochando, I. Pastor, M. A. Pedrosa, D. Tafalla, L. García, R. Sánchez, A. Petrov, K. Sarksian, and N. Skvortsova, Nucl. Fusion **42**, 787 (2002).

[10]Y. H. Xu, S. Jachmich, R. R. Weynants, and TEXTOR team, Plasma Phys. Controlled Fusion **47**, 1841 (2005).

[11]T. A. Carter, Phys. Plasmas **13**, 010701 (2006).

[12]H. Tsuchiya, T. Morisaki, V. P. Budaev, A. Komori, H. Yamada, and LHD Experimental Group, Plasma Fusion Res. **5**, S2078 (2010).

[13]X. Garbet and R. E. Waltz, Phys. Plasmas **5**, 2836 (1998).

[14]J. A. Mier, L. García, and R. Sánchez, Phys. Plasmas **13**, 102308 (2006).

[15]Y. Idomura, H. Urano, N. Aiba, and S. Tokuda, Nucl. Fusion **49**, 065029 (2009).

[16]T. Görler, X. Lapillonne, S. Brunner, J. Chowdhury, T. Dannert, F. Jenko, B. F. McMillan, F. Merz, D. Told, and L. Villard, J. Phys.: Conf. Ser. **260**, 012011 (2010).

[17]Y. Sarazin, V. Grandgirard, J. Abiteboul, S. Allfrey, X. Garbet, Ph. Ghendrih, G. Latu, A. Strugarek, G. Dif-Pradalier, P. H. Diamond, S. Ku, C. S. Chang, B. F. McMillan, T. M. Tran, L. Villard, S. Jolliet, A. Bottino, and P. Angelino, Nucl. Fusion **51**, 103023 (2011).

[18]G. Dif-Pradalier, P. H. Diamond, V. Grandgirard, Y. Sarazin, J. Abiteboul, X. Garbet, Ph. Ghendrih, A. Strugarek, S. Ku, and C. S. Chang, Phys. Rev. E **82**, 025401(R) (2010).

[19]R. E. Waltz and J. Candy, Phys. Plasmas **12**, 072303 (2005).

[20]Z. H. Wang, P. H. Diamond, Ö. D. Gürcan, X. Garbet, and X. G. Wang, Nucl. Fusion **51**, 073009 (2011).

[21]P. Bak, C. Tang, and K. Weisenfeld, Phys. Rev. Lett. **59**, 381 (1987).

[22]P. H. Diamond and T. S. Hahm, Phys. Plasmas **2**, 3643 (1995).

[23]D. E. Newman, B. A. Carreras, P. H. Diamond, and T. S. Hahm, Phys. Plasmas **3**, 1858 (1996).

[24]B. A Carreras, D. Newman, V. E. Lynch, and P. H. Diamond, Phys. Plasmas **3**, 2903 (1996).

[25]T. Hwa and M. Kardar, Phys. Rev. A **45**, 7002 (1992).

[26]B. A. Carreras, V. E. Lynch, D. E. Newman, and G. M. Zaslavsky, Phys. Rev. E **60**, 4770 (1999).

[27]I. Gruzinov, P. H. Diamond, and M. N. Rosenbluth, Phys. Rev. Lett. **89**, 255001 (2002).

[28]D. E. Newman, R. Sánchez, B. A. Carreras, and W. Ferenbaugh, Phys. Rev. Lett. **88**, 204304 (2002).

[29]R. Sánchez, D. E. Newman, B. A. Carreras, R. Woodard, W. Ferenbaugh, and H. R. Hicks, Nucl. Fusion **43**, 1031 (2003).

[30]M. Yagi, T. Ueda, S.-I. Itoh, M. Azumi, K. Itoh, P. H. Diamond, and T. S. Hahm, Plasma Phys. Controlled Fusion **48**, A409 (2006).

[31]P. Beyer, S. Benkadda, X. Garbet, and P. H. Diamond, Phys. Rev. Lett. **85**, 4892 (2000).

[32]S. Benkadda, P. Beyer, N. Bian, C. Figarella, O. Garcia, X. Garbet, P. Ghendrih, Y. Sarazin, and P. H. Diamond, Nucl. Fusion **41**, 995 (2001).

[33]R. Sanchez, D. E. Newman, and B. A. Carreras, Nucl. Fusion **41**, 247 (2001).

[34]X. Garbet, C. Bourdelle, G. T. Hoang, P. Maget, S. Benkadda, P. Beyer, C. Figarella, I. Vitsekhovitch, O. Agullo, and N. Bian, Phys. Plasmas **8**, 2793 (2001).

[35]S. S. Kim, H. Jhang, P. H. Diamond, L. Terzolo, S. M. Yi, and T. S. Hahm, Nucl. Fusion **51**, 073021 (2011).

[36]J. Candy, R. E. Waltz, and M. N. Rosenbluth, Phys. Plasmas **11**, 1879 (2004).

[37]Y. Sarazin, A. Strugarek, G. Dif-Pradalier, J. Abiteboul, S. Allfrey, X. Garbet, P. Ghendrih, and G. Latu, J. Phys.: Conf. Ser. **260**, 012017 (2010).

[38]H. Jhang, S. S. Kim, and P. H. Diamond, J. Korean Phys. Soc. **61**, 55 (2012).

[39]E. J. Powers, Nucl. Fusion **14**, 749 (1974).

[40]W. X. Wang, T. S. Hahm, W. W. Lee, G. Rewoldt, J. Manickam, and W. M. Tang, Phys. Plasmas **14**, 072306 (2007).

[41]E.-j. Kim and P. H. Diamond, Phys. Rev. Lett. **90**, 185006 (2003).

[42]M. N. Rosenbluth and F. L. Hinton, Phys. Rev. Lett. **80**, 724–727 (1998).

[43]L. Schmitz, L. Zeng, T. L. Rhodes, J. C. Hillesheim, E. J. Doyle, R. J. Groebner, W. A. Peebles, K. H. Burrell, and G. Wang, Phys. Rev. Lett. **108**, 155002 (2012).

[44]T. Estrada, C. Hidalgo, T. Happel, and P. H. Diamond, Phys. Rev. Lett. **107**, 245004 (2011).

[45]G. S. Xu, B. N. Wan, H. Q. Wang, H. Y. Guo, H. L. Zhao, A. D. Liu, V. Naulin, P. H. Diamond, G. R. Tynan, M. Xu, R. Chen, M. Jiang, P. Liu, N. Yan, W. Zhang, L. Wang, S. C. Liu, and S. Y. Ding, Phys. Rev. Lett. **107**, 125001 (2011).

[46]H. E. Hurst, Trans. Am. Soc. Civ. Eng. **116**, 770 (1951).

[47]M. Gilmore, C. X. Yu, T. L. Rhodes, and W. A. Peebles, Phys. Plasmas **9**, 1312 (2002).

[48]A. Scipioni, P. Rischette, G. Bonhomme, and P. Devynck, Phys. Plasmas **15**, 112303 (2008).

[49]J. L. McCauley, G. H. Gunaratne, and K. E. Bassler, Physica A **379**, 1–9 (2007).

[50]B. B. Mandelbrot and J. R. Wallis, Water Resour. Res. **4**, 909–918, doi:10.1029/WR004i005p00909 (1968).

[51]M. Aschwanden, *Self-Organized Criticality in Astrophysics* (Springer-Verlag, Berlin, Heidelberg, 2011), pp. 139–149.

[52]R. Sánchez, D. E. Newman, W. Ferenbaugh, B. A. Carreras, V. E. Lynch, and B. Ph. van Milligen, Phys. Rev. E **66**, 036124 (2002).

[53]W. W. Xiao, P. H. Diamond, W. C. Kim, S. W. Yoon, J. Kim, S. H. Hahn, G. S. Yun, J. G. Bak, Y. U. Nam, J. W. Ahn, H. K. Kim, H. T. Kim, K. P. Kim, H. K. Park, G. H. Choe, M. J. Choi, J. I. Song, S. G. Lee, T. Rhee, J. M. Kwon, K. D. Lee, W. H. Ko, S. I. Park, M. Jung, Y. S. Bae, Y. K. Oh, and KSTAR team, "First signatures of ELM mitigation by supersonic molecular beam injection in KSTAR," Phys. Rev. Lett (submitted).

[54]K. W. Gentle, W. L. Rowan, R. V. Bravenec, G. Cima, T. P. Crowley, H. Gasquet, G. A. Hallock, J. Heard, A. Ouroua, P. E. Phillips, D. W. Ross, P. M. Schoch, and C. Watts, Phys. Rev. Lett. **74**, 3620 (1995).

[55]H. J. Sun, P. H. Diamond, Z. B. Shi, C. Y. Chen, L. H. Yao, X. T. Ding, B. B. Feng, X. L. Huang, Y. Zhou, J. Zhou, X. M. Song, and HL-2A Team, Nucl. Fusion **51**, 113010 (2011).

[56]K. Ida, M. Yoshinuma, K. Nagaoka, M. Osakabe, S. Morita, M. Goto, M. Yokoyama, H. Funaba, S. Murakami, K. Ikeda, H. Nakano, K. Tsumori, Y. Takeiri, O. Kaneko, and LHD Experiment Group, Nucl. Fusion **50**, 064007 (2010).

[57]S. Ku, J. Abiteboul, P. H. Diamond, G. Dif-Pradalier, J. M. Kwon, Y. Sarazin, T. S. Hahm, X. Garbet, C. S. Chang, G. Latu, E. S. Yoon, Ph. Ghendrih, S. Yi, A. Strugarek, W. Solomon, and V. Grandgirard, Nucl. Fusion **52**, 063013 (2012).

[58]S. S. Kim, H. Jhang, and P. H. Diamond, Phys. Plasmas **19**, 084502 (2012).

[59]Y. Nagashima, S.-I. Itoh, S. Inagaki, H. Arakawa, N. Kasuya, A. Fujisawa, K. Kamataki, Y. Yamada, S. Shinohara, S. Oldenbürger, M. Yagi, Y. Takase, P. H. Diamond, and K. Itoh, Phys. Plasmas **18**, 070701 (2011).